Supplementary Information (SI) for Journal of Materials Chemistry A.

Supporting Information

Defective Ceria as a Structural and Electronic Modifier of Nitrogen-Doped Carbon and Cobalt-Nitrogen-Carbon Electrocatalysts for Oxygen Reduction in Alkaline Electrolyte

Wajdi Alnoush, Navid Noor, Shayan Angizi, Amirhossein Raksha, Thomas Baker, and Drew Higgins*

Wajdi Alnoush, Chemical Engineering Department, McMaster University
1280 Main St W, Hamilton, ON L8S 4L8, Canada.
alnoushw@mcmaster.ca

Navid Noor, Chemical Engineering Department, McMaster University
1280 Main St W, Hamilton, ON L8S 4L8, Canada.
noormohn@mcmaster.ca

Shayan Angizi, Chemical Engineering Department, McMaster University
1280 Main St W, Hamilton, ON, L8S 4L8, Canada.
angizis@mcmaster.ca

Amirhossein Raksha, Chemical Engineering Department, McMaster University
1280 Main St W, Hamilton, ON, L8S 4L8, Canada.
rakhsha@mcmaster.ca

Thomas Baker, Chemical Engineering Department, McMaster University
1280 Main St W, Hamilton, ON, L8S 4L8, Canada.
bakert4@mcmaster.ca

*Drew Higgins, Chemical Engineering Department, McMaster University
1280 Main St W, Hamilton, ON, L8S 4L8, Canada.
higgid2@mcmaster.ca

Note S1 – Crystallite size and interplanar spacing estimation from XRD patterns using Sherrer's equation and Bragg's law

To determine the average crystallite size (D), the Scherrer equation was used:

$$D = \frac{K \cdot \lambda}{(FWHM \ \cdot cos\theta)} \qquad \text{Equation. S1}$$

where K is the Scherrer constant (0.64), λ is the wavelength of the X-ray radiation (1.541 Å, Cu Kα_1), FWHM is the peak's full width at half maximum, and θ is the Bragg angle (in radians). The reported Scherrer crystallite sizes reported herein are based on the observed FWHM values without instrumental broadening correction. Accordingly, the analysis is employed to compare relative changes in apparent crystallite size across the sample series, rather than to provide absolute size values.

Furthermore, to estimate the interplanar spacing (d-spacing), Bragg's law was used:

$$d - spacing = \frac{n \cdot \lambda}{2 \cdot sin\theta} \qquad \text{Equation. S2}$$

where n is the order of reflection (1), λ is the wavelength of the X-ray radiation (1.541 Å, Cu Kα_1), and θ is the Bragg angle (in degrees)

Note S2 – g-factor determination from EPR spectra

The position of the EPR resonance is characterized by the g-factor, which is sensitive to ligand field and symmetry around the paramagnetic Ce^{3+}. The g-factor was determined using the Gaussian fits of the baseline-corrected EPR spectra according to the following equation:

$$g - factor = \frac{h \cdot v}{\mu_B \cdot B_0} \qquad \text{Equation. S3}$$

where h is Planck's constant (6.625×10^{-34} $m^2 \cdot kg/s$), v is the microwave frequency (9.45 GHz), μ_B is Bohr magneton (9.274×10^{-24} $A \cdot m^2$), and B_0 is the applied resonant magnetic field.

Note S3 – Electrochemically active surface area (ECSA) determination

The double-layer capacitance (C_{dl}) method was used for estimating the electrochemically active surface area (ECSA). In Ar-saturated 0.1 M KOH, cyclic voltammograms (CVs) were collected at different scan rates (5-100 mV/s) in the non-Faradic region (0.9-1.0 V vs. RHE). For each CV, the difference between the anodic and cathodic current densities at the mid-potential was calculated and plotted as a function of the scan rate, and the C_{dl} was estimated from the slope. We used the specific capacitance (C_s) value of 0.02 mF/cm^2 in our calculations.[1, 2] Using the mass loading of the catalyst (m_{cat}), ECSA was then determined as follows:

$$ECSA = \frac{C_{dl}}{C_s \times m_{cat}} \qquad \text{Equation. S4}$$

It is worth noting that the utilized C_s value is typical for carbonaceous materials, which is the dominant phase of the studied ceria@N-C and ceria@Co/N-C catalysts. While the absolute ECSA values depend on the assumed C_s, the use of a constant C_s across all samples enables reliable relative comparisons of electrochemically accessible surface area within this study.

Note S4 – Equivalent circuit modeling of electrochemical impedance spectroscopy (EIS)

Fitting procedure

EIS spectra were fitted with an equivalent circuit model accounting for solution resistance (R_s), interfacial charge-transfer resistance (R_{ct}), non-ideal capacitive behavior via a constant phase element (CPE), and mixed semi-infinite (W) and finite (W_o) Warburg diffusion elements. To ensure the reliability of the EIS analysis, multiple equivalent circuit models were systematically evaluated, including Randles-type circuits and models with finite and infinite Warburg elements. Final circuit selection was based on optimal fit quality (minimized root-mean-square error) and physical interpretability.

Summary of results

At the low-frequency tail, the prepared electrocatalysts displayed distinct diffusion behaviors. Among ceria@N-C samples, V_o-rich prCeO_2@N-C and trCeO_2@N-C exhibited less steep Warburg tails and reduced finite Warburg resistance (W_o) of 0.05 and 0.045 Ω, respectively, compared to 0.072 Ω for CeO_2@N-C, indicating enhanced ionic transport through defect-mediated pathways. Interestingly, this vacancy-driven diffusion improvement was only observed in ceria@N-C samples, whereas metallic Co NPs in ceria@Co/N-C samples alter ion-transport pathways and obscure vacancy-enabled diffusion gains, evident from their significantly higher W_o values. The semi-infinite Warburg coefficient (W) also showed support-dependent trends. Ceria@N-C samples exhibited lower W values (≈52-74 $\Omega\cdot s^{-1/2}$) than pristine N-C (105.9 $\Omega\cdot s^{-1/2}$), consistent with reduced diffusion impedance and more accessible ion-transport pathways upon ceria incorporation. In contrast, ceria@Co/N-C series displayed larger W values (55-137 $\Omega\cdot s^{-1/2}$), indicating metallic Co NPs and the associated microstructural changes introduce additional transport resistance that overshadows vacancy-driven diffusion improvements. The CPE parameters reflect subtle interface differences, where ceria@N-C and ceria@Co/N-C electrocatalysts generally exhibiting higher CPE constants ($\sim 10^{-7}$ $\Omega^{-1}\cdot s^{\alpha}$) and slightly smaller exponents (α=0.84-0.89) compared to ceria-free N-C (6.12×10^{-8} $\Omega^{-1}\cdot s^{\alpha}$, α=0.92) and Co/N-C (6.93×10^{-8} $\Omega^{-1}\cdot s^{\alpha}$, α=0.91), reflecting a more heterogeneous interfacial structure upon ceria integration.

Additionally, Bode magnitude and phase angle plots (Figs. S11a and S11b) for individual catalyst components (i.e., CeO_2, N-C, and Co/N-C) and ceria@N-C catalysts (i.e., CeO_2@N-C, prCeO_2@N-C, and trCeO_2@N-C) corroborate observations from Nyquist plots. At low frequencies, CeO_2 exhibited the highest impedance (> 3 Ω) and lowest phase angle (< 20°), indicative of its poor charge transfer. In contrast, N-C and Co/N-C started from a lower impedance of ~2.9 Ω at 0.1 Hz that progressively decreased to ~1.8 Ω at 10 Hz, while phase angles started high (> 70°) at 0.1 Hz and progressively dropped to < 20° at 10 Hz. At intermediate frequencies, CeO_2 exhibited a broad peak, consistent with sluggish electron/ion migration, while the phase response for N-C and Co/N-C was flattened, suggesting better charge transfer kinetics and improved capacitive-to-resistive transition. For ceria@N-C electrocatalysts, CeO_2@N-C exhibited the highest impedance among at the low frequency region, followed by V_o-rich trCeO_2@N-C and prCeO_2@N-C. A similar trend was observed for phase angles, with the trend following CeO_2@N-C > trCeO_2@N-C > prCeO_2@N-C, indicating enhanced charge transfer in samples embedding defective ceria.

Note S5 – Collection efficiency (N) in the RRDE tip

The collection efficiency (N) of the ring was calibrated using potassium ferricyanide. First, 1 M KCl with 10 mM $K_3[Fe(CN)_6]$ electrolyte was prepared and Ar-saturated. Then, voltammograms were collected in a 3-electrode cell with a Ag/AgCl (saturated KCl) reference electrode and a graphite rod counter electrode. The potential at the disk was scanned from 1-0.4 V vs. RHE, whereas the potential of the ring was fixed. Thus, $Fe^{3+} \rightarrow Fe^{2+}$ reduction occurred at the disk while $Fe^{2+} \rightarrow Fe^{3+}$ oxidation occurred at the ring. The collection efficiency (N) was then determined as follows:

$$N = -\frac{I_{Ring}}{I_{Disk}} \qquad \text{Equation. S5}$$

Note S6 – ECSA-normalized activity

The ECSA-normalized activity (j_{ECSA}) of the catalysts was calculated at 0.75 V vs. RHE according to the following equation:

$$j_{ECSA} = \frac{j_k}{ECSA} \qquad \text{Equation. S6}$$

where j_k is the kinetic current density determined from the Koutecký-Levich equation [3]:

$$\frac{1}{j_k} = \frac{1}{j} - \frac{1}{j_d} \qquad \text{Equation. S7}$$

Where j is the current density and j_d is the diffusion-limited current density.

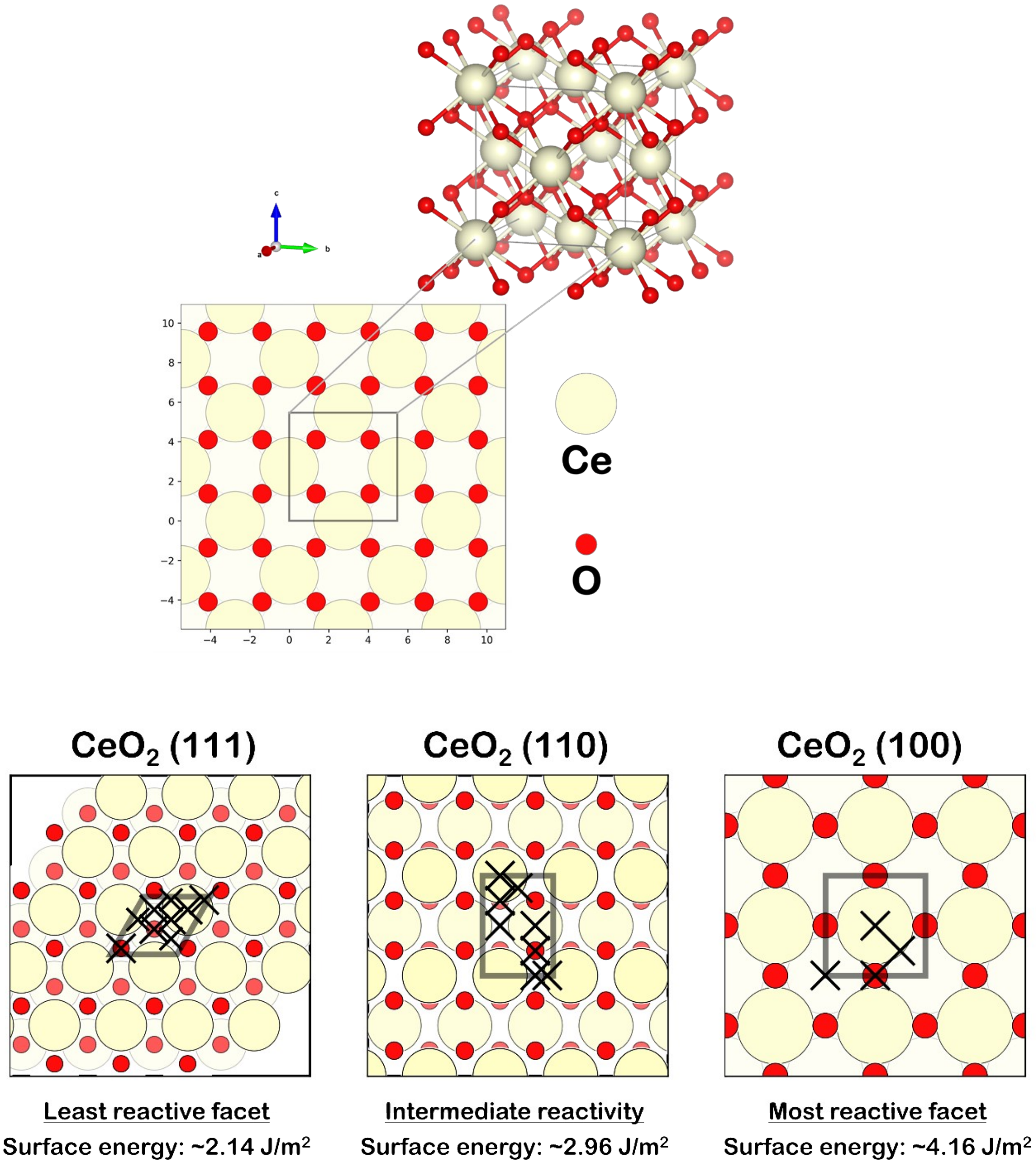

Figure S1. Crystal structure of fluorite CeO_2. Bottom panel: structures and surface energies of the (111), (100), and (110) facets of CeO_2. The (100) facet is equivalent to (200), while the (11) facet is equivalent to (220). Crosses (×) denote potential adsorption sites.

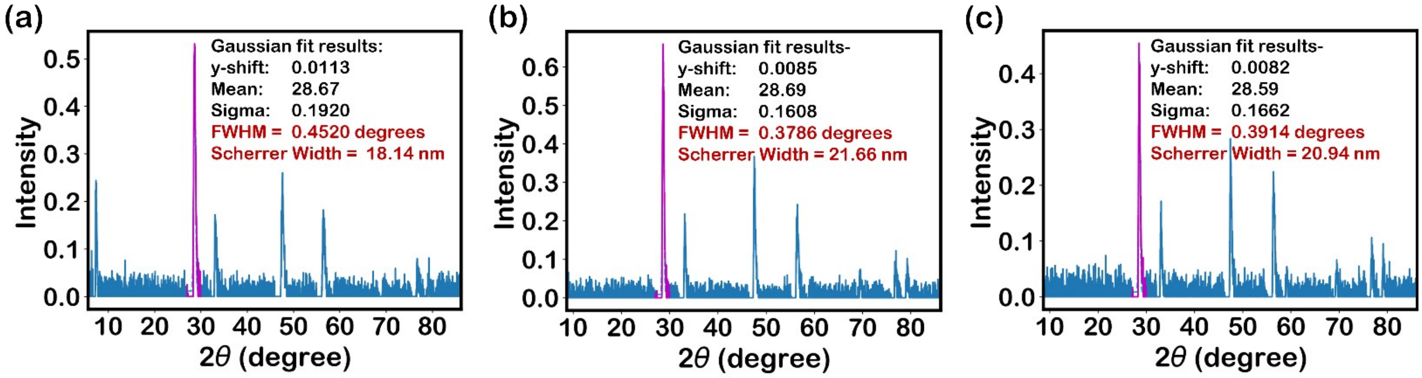

Figure S2. Crystallite size (Scherrer width) determination from XRD diffraction patterns of CeO_2, prCeO_2, and trCeO_2. Diffraction patterns and fitted (111) peak of (a) CeO_2, (b) prCeO_2, and (c) trCeO_2.

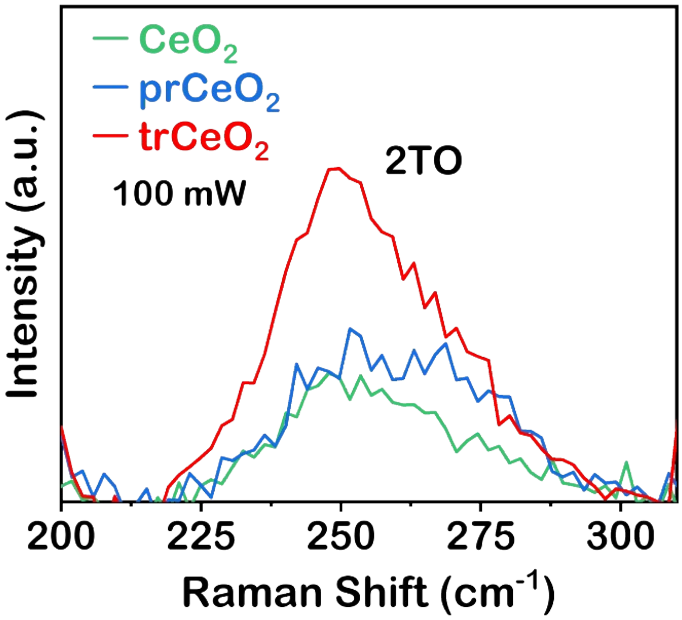

Figure S3. Raman spectra of the 2TO band region of CeO$_2$, prCeO$_2$, and trCeO$_2$.

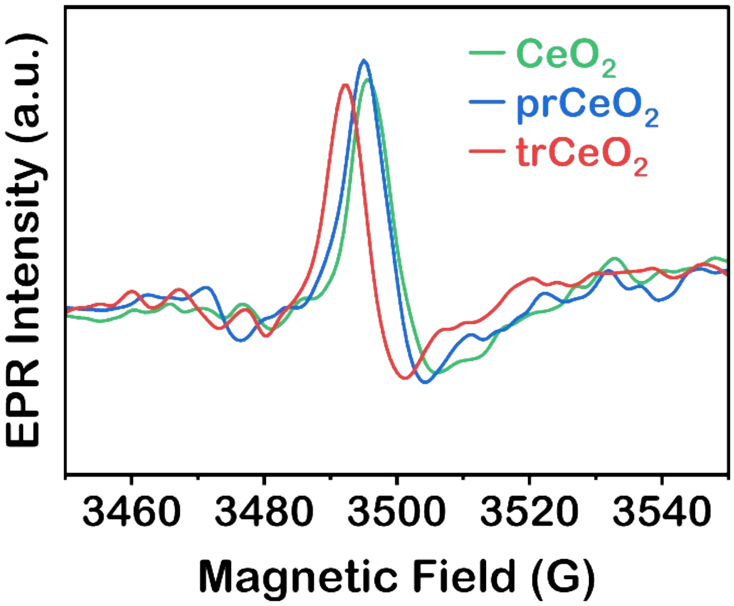

Figure S4. Baseline-corrected EPR spectra of CeO$_2$, prCeO$_2$, and trCeO$_2$ precursors.

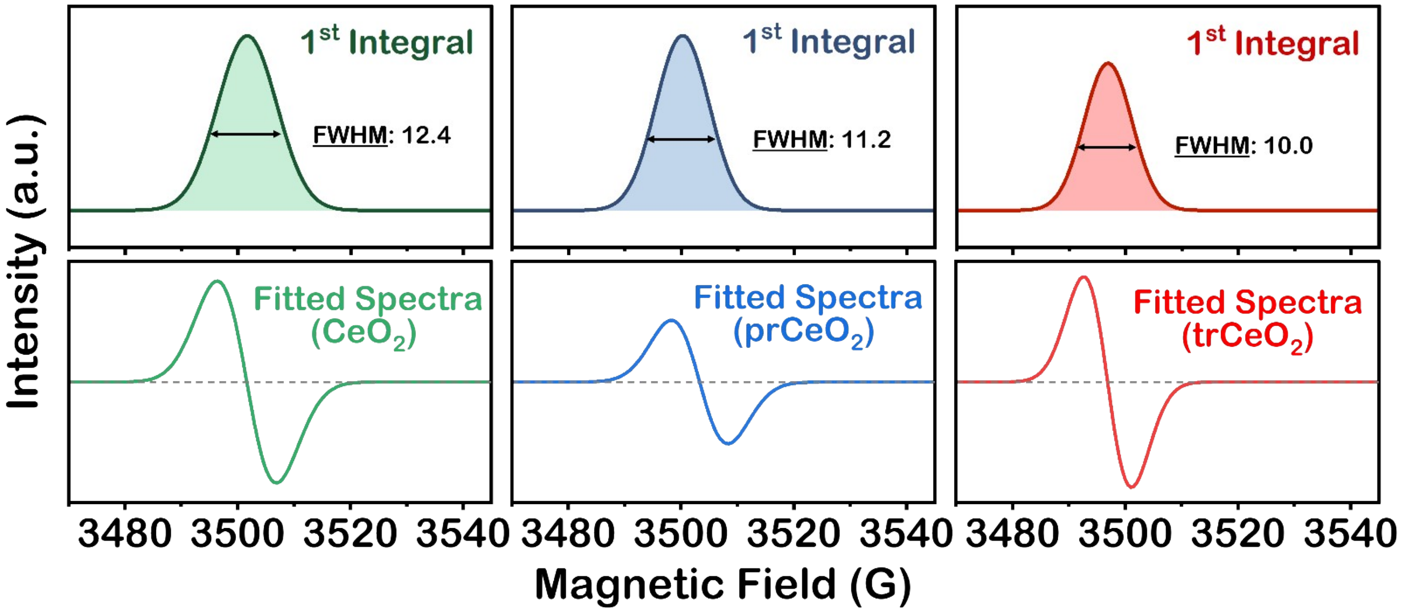

Figure S5. Gaussian fitting (bottom panel) and the corresponding integration (top panel) of the EPR spectra of CeO_2, $prCeO_2$, and $trCeO_2$ precursors.

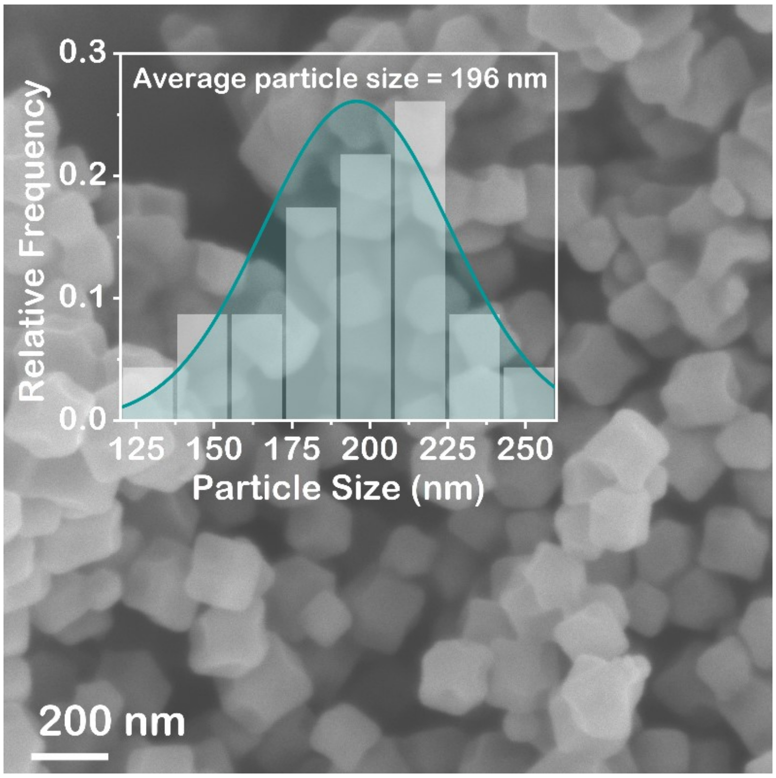

Figure S6. SEM of Zn-ZIF8 particles.

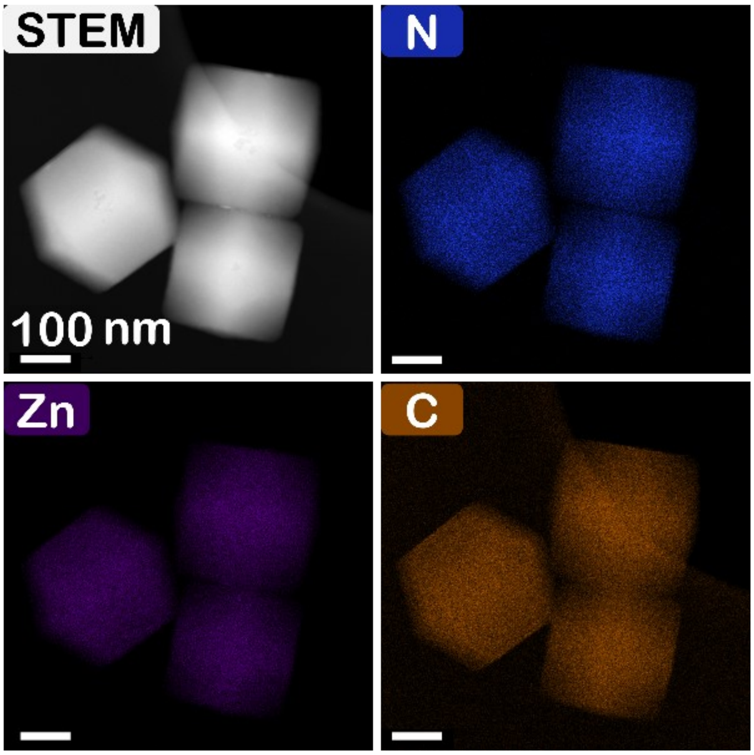

Figure S7. STEM-EELS of Zn-ZIF8 particles. Elemental maps show a uniform distribution of Zn, N, and C.

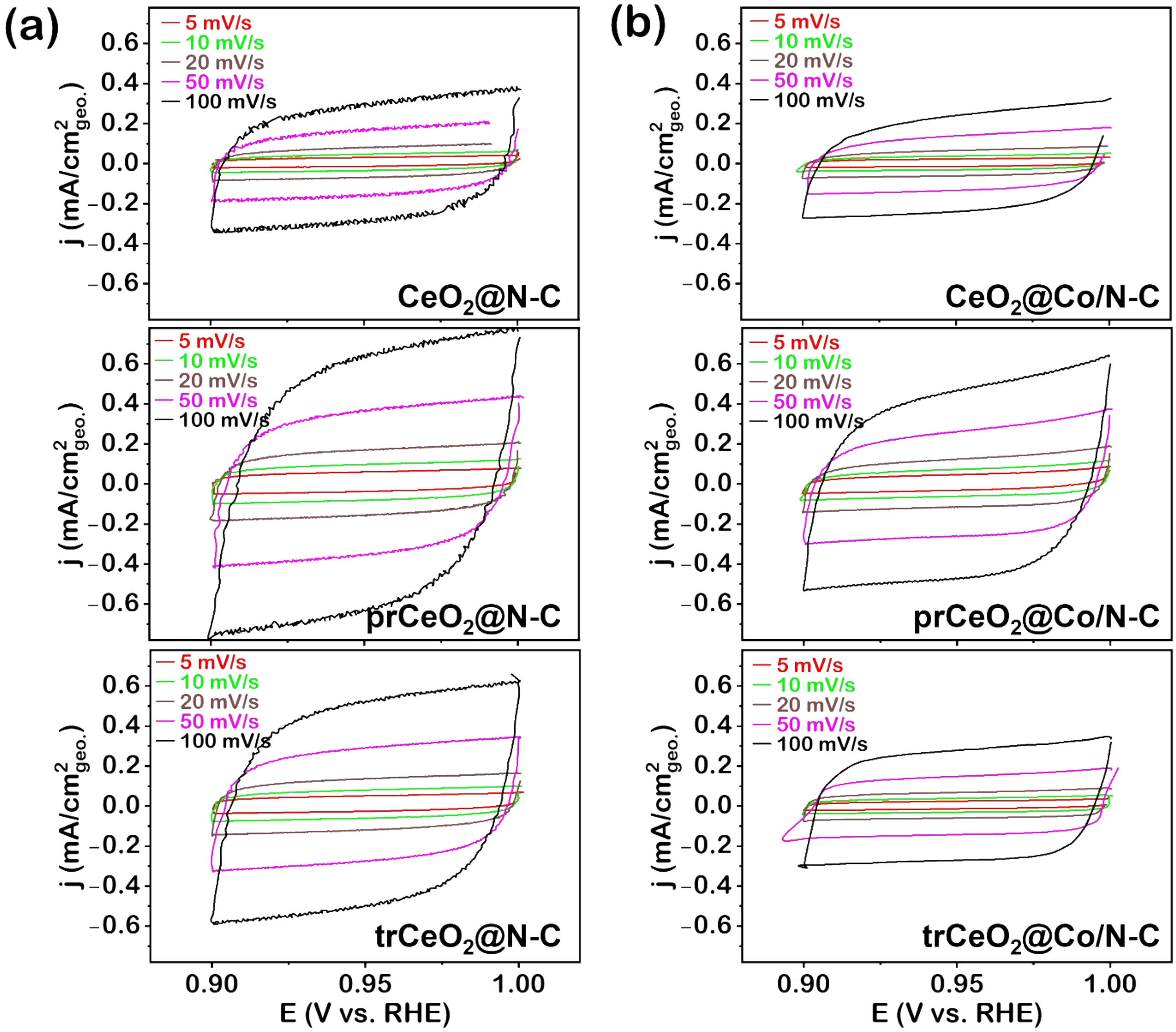

Figure S8. CVs in the non-Faradaic region in 0.1 M KOH for ECSA determination. Panel (a) displays the CVs of catalysts derived from Zn-ZIF8 (CeO$_2$@N-C, prCeO$_2$@N-C, and trCeO$_2$@N-C). Panel (b) displays the CVs of catalysts derived from Co/Zn-ZIF (CeO$_2$@Co/N-C, prCeO$_2$@Co/N-C, and trCeO$_2$@Co/N-C).

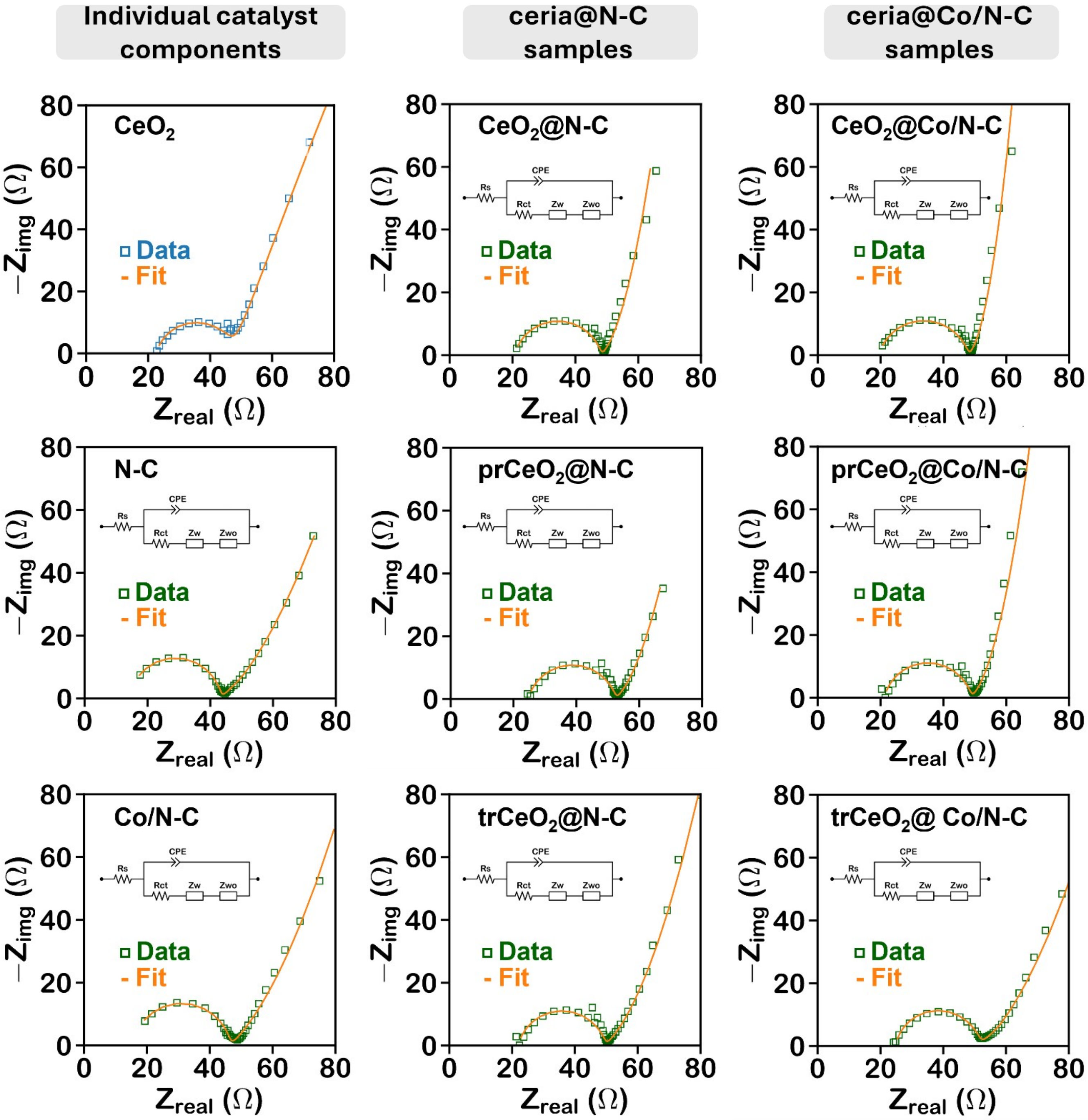

Figure S9. Fitted EIS Nyquist Plots.

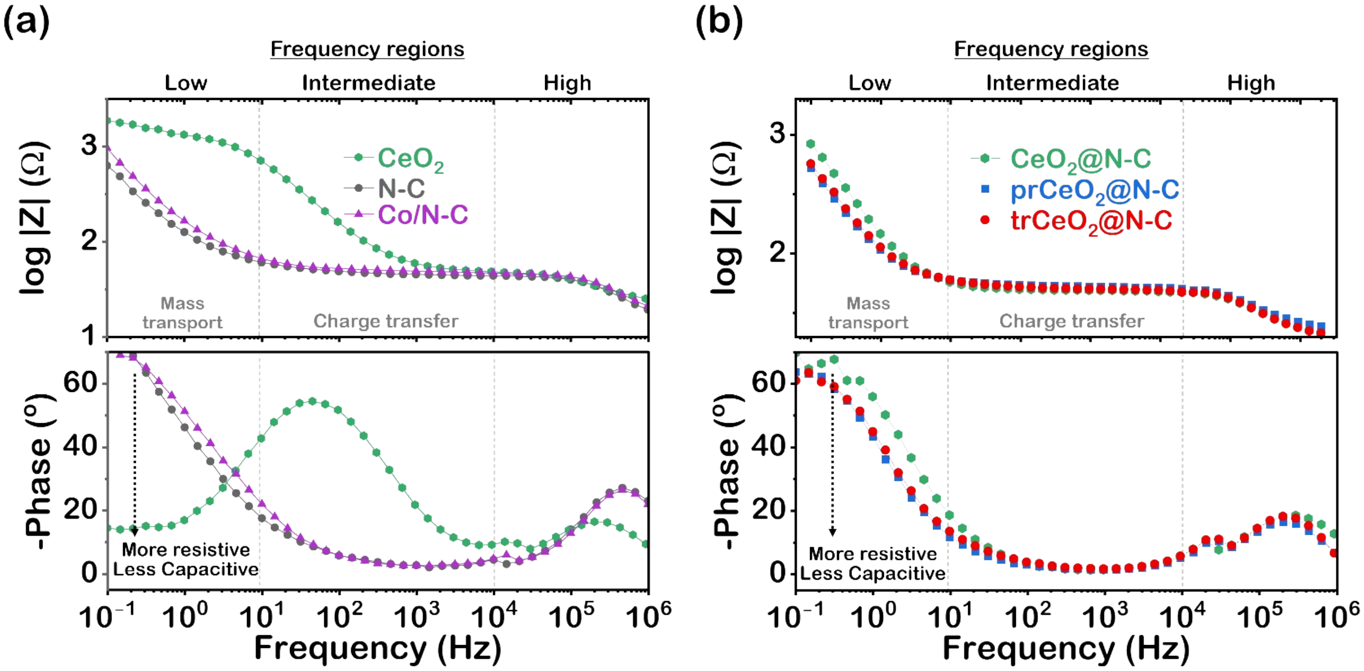

Figure S10. EIS Bode magnitude (top) and phase angle (bottom) plots of (a) isolated catalyst components (CeO$_2$, N-C, and Co/N-C). (b) ceria@N-C electrocatalysts (CeO$_2$@N-C, prCeO$_2$@N-C, and trCeO$_2$@N-C).

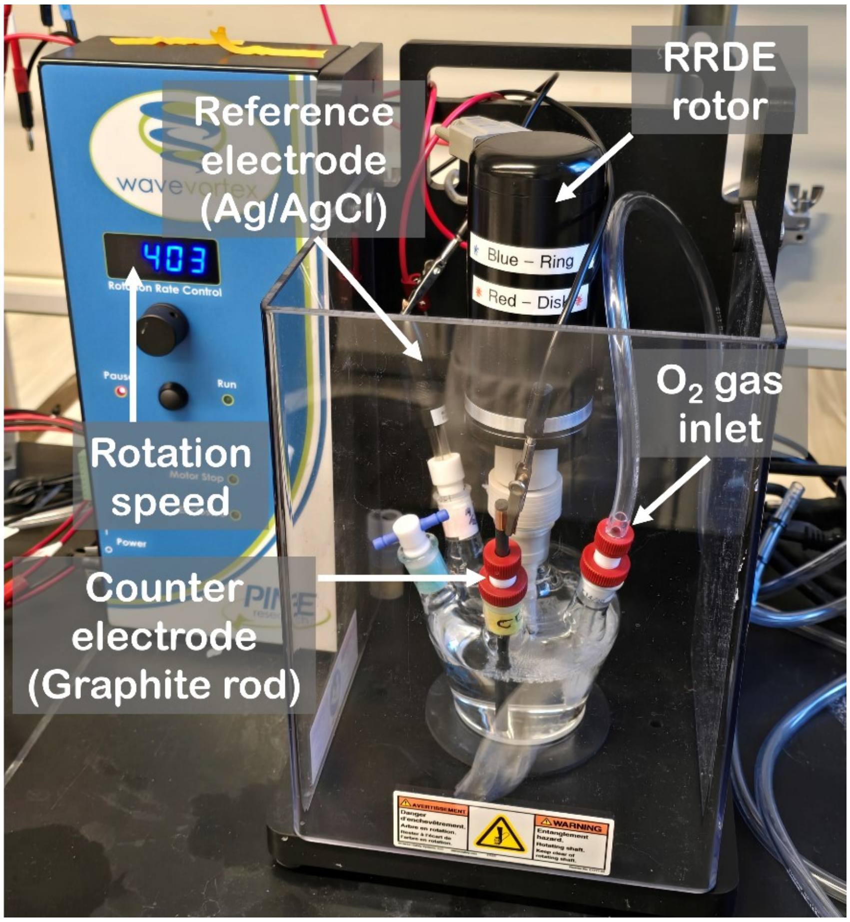

Figure S11. Rotating ring-disk electrode (RRDE) setup for performance evaluation of ORR catalysts. The catalyst is deposited on a glassy carbon disk electrode (0.2 mg/cm^2), and H_2O_2 generated is detected at a Pt ring.

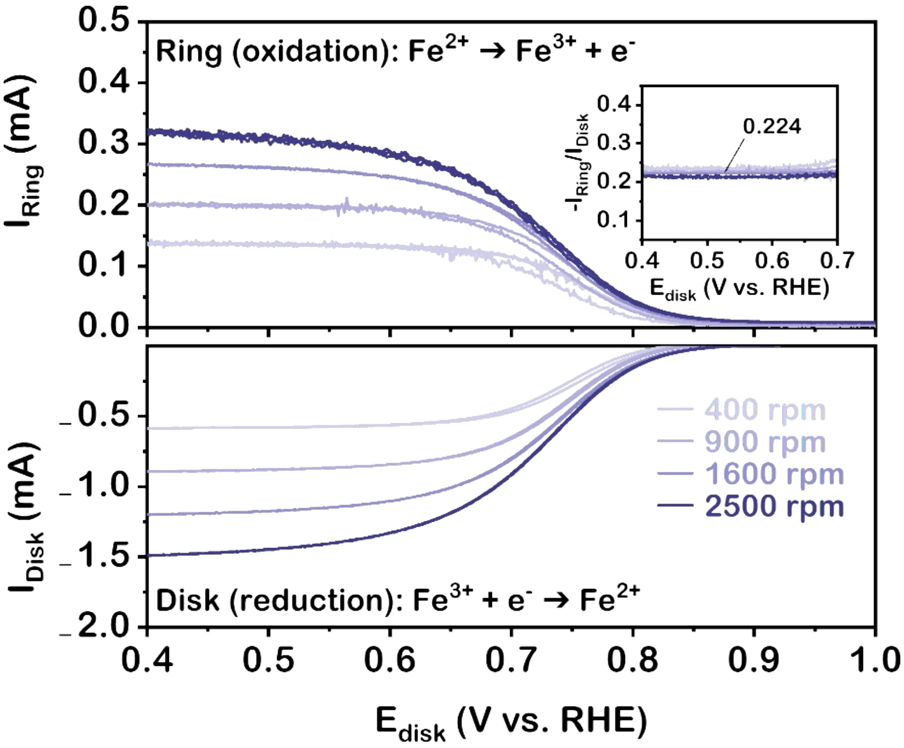

Figure S12. Ring collection efficiency (N) determined from the redox of potassium ferricyanide ($K_3[Fe(CN)_6]$). Voltammograms were collected at 400, 900, 1600, and 2500 rpm in Ar-saturated 1 M KCl with 10 mM $K_3[Fe(CN)_6]$. The inset shows the corresponding collection efficiency between 0.4 and 0.7 V vs. RHE.

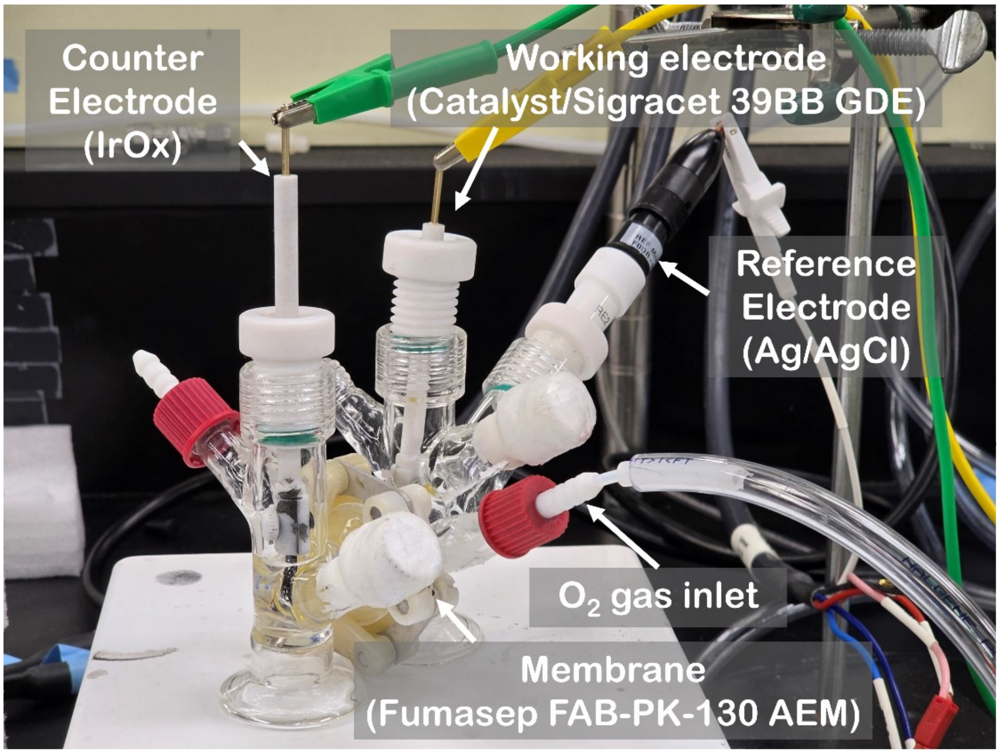

Figure S13. Two-compartment H-Cell setup used for H_2O_2 quantification. Chronoamperometry tests were run in 0.1 M KOH using a working electrode geometric area of 0.5 cm^2. The total electrolyte volume used is 22 mL, where 1 mL sample from the catholyte is withdrawn for H_2O_2 quantification.

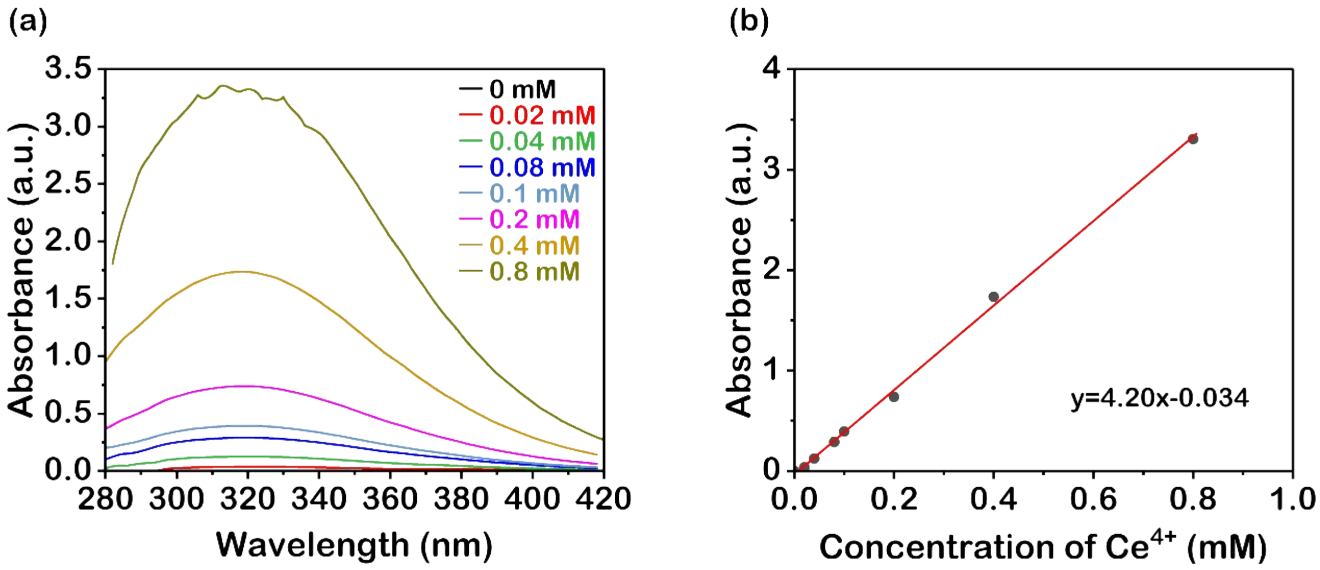

Figure S14. (a) UV-Vis spectra for 0-0.8 mM $CeSO_4$ in 0.5 M H_2SO_4. (b) The corresponding calibration curve used for H_2O_2 quantification from H-Cell tests.

Table S1. FWHM values extracted from XRD diffraction peaks of CeO_2, $prCeO_2$, and $trCeO_2$.

Precursor	Reflection (hkl)	2θ (°)	FWHM
CeO_2	111	28.57	0.5923
	200	33.07	0.5599
	220	47.54	0.7562
$prCeO_2$	111	28.65	0.4447
	200	33.16	0.4517
	220	47.56	0.4621
$trCeO_2$	111	28.50	0.4980
	200	33.01	0.4769
	220	47.45	0.5004

Table S2. Average crystallite size (D) values estimated from the (111) reflection in XRD patterns of CeO_2, prCeO_2, and trCeO_2.

Precursor	D/Scherrer Width (nm)
CeO_2	18.14
prCeO_2	21.66
trCeO_2	20.94

Table S3. Interplanar distance (d-spacing) values estimated from XRD patterns of CeO_2, $prCeO_2$, and $trCeO_2$.

Precursor	Reflection (hkl)	2θ (°)	d-spacing (Å) (Cu Kα)
CeO_2	111	28.57	3.12
	200	33.07	2.71
	220	47.54	1.91
$prCeO_2$	111	28.65	3.11
	200	33.16	2.70
	220	47.56	1.91
$trCeO_2$	111	28.50	3.13
	200	33.01	2.71
	220	47.45	1.92

Table S4. EPR cavity Q-factor and peak-to-peak widths for CeO_2, $prCeO_2$, and $trCeO_2$.

Sample	Q-factor	Peak-to-Peak width (G)
CeO_2	4316	10.5
$prCeO_2$	3993	9.5
$trCeO_2$	3614	8.6

Table S5. Values of C_{dl} and electrochemically active surface area (ECSA) obtained from the C_{dl} method.

Catalyst	C_{dl} (mF/cm^2)	ECSA (m^2/g)
CeO_2	0.13	3.25
N-C	8.5	212.5
CeO_2@N-C	5.5	137.5
prCeO_2@N-C	12.4	310
trCeO_2@N-C	9.9	247.5
Co/N-C	8.8	220
CeO_2@Co/N-C	4.6	115
prCeO_2@Co/N-C	9.1	227.5
trCeO_2@Co/N-C	5.4	135

Table S6. Fitting parameters for EIS Nyquist plots.

Catalyst	R_s (Ω)	R_{ct} (Ω)	CPE ($\Omega^{-1} \cdot s^{\alpha}$)	α	W ($\Omega \cdot s^{-1}/2$)	W_o (Ω)
N-C	14.4	29.0	6.12e-08	0.92	105.9	2.942
CeO_2@N-C	20.7	27.5	2.70e-07	0.85	57.34	0.072
prCeO_2@N-C	24.7	27.8	3.88e-07	0.84	51.68	0.050
trCeO_2@N-C	21.9	27.7	1.97e-07	0.89	74.02	0.045
Co/N-C	15.6	30.9	6.93e-08	0.91	121.3	0.465
CeO_2@Co/N-C	19.5	28.4	3.05e-07	0.84	55.07	0.145
prCeO_2@Co/N-C	21.3	27.5	3.69e-07	0.85	55.14	0.859
trCeO_2@Co/N-C	24.9	26.7	1.97e-07	0.89	137.4	2.945

Catalyst	R_s (Ω)	R_1 (Ω)	CPE_1 ($\Omega^{-1} \cdot s^{\alpha 1}$)	α1	R_2 (Ω)	CPE_2 ($\Omega^{-1} \cdot s^{\alpha 2}$)	α2	W ($\Omega \cdot s^{-1}/2$)
CeO_2	22.6	24.0	3.67e-07	0.85	24.0	4.33e-05	0.82	235

* $R_{ct} = R_1 + R_2$

Table S7. ECSA-normalized activity.

Catalyst	j (mA/cm^2) @0.75 V	j_d (mA/cm^2)	j_k (mA/cm^2)	j_{ECSA} (μA/cm^2)
N-C	0.29	3.58	0.316	0.146
CeO_2@N-C	0.07	4.06	0.066	0.044
prCeO_2@N-C	0.17	4.08	0.174	0.055
trCeO_2@N-C	0.15	3.79	0.159	0.063
Co/N-C	3.17	5.15	8.245	3.673
CeO_2@Co/N-C	0.87	4.79	1.063	0.903
prCeO_2@Co/N-C	1.51	4.74	2.216	0.956
trCeO_2@Co/N-C	1.24	4.68	1.687	1.237

Table S8. H_2O_2 yield rate after 30-minute chronoamperometry at 0.1 V vs. RHE.

Catalyst	$[H_2O_2]$	Yield rate (mmol g_{cat}^{-1} h^{-1})
Carbon paper (CP)	3.57	0.31
N-C	4.92	0.44
$prCeO_2$@N-C	3.18	0.28
$trCeO_2$@N-C	4.67	0.41

References

1. C. C. L. McCrory, S. Jung, J. C. Peters and T. F. Jaramillo, Benchmarking Heterogeneous Electrocatalysts for the Oxygen Evolution Reaction, 2013, https://doi.org/10.1021/ja407115.
2. T. A. Centeno and F. Stoeckli, On the specific double-layer capacitance of activated carbons, in relation to their structural and chemical properties, *Journal of Power Sources*, 2006, 154.
3. A. J. Bard and L. R. Faulkner, *Electrochemical methods: fundamentals and applications*, 2001.